Multiscale Atmospheric Overturning of the Indian Summer Monsoon as Seen through Isentropic Analysis

Xingchao Chen

Department of Meteorology and Atmospheric Science, and Center for Advanced Data Assimilation and Predictability Techniques, The Pennsylvania State University, University Park, Pennsylvania, and Center for Prototype Climate Modeling, New York University Abu Dhabi, Abu Dhabi, United Arab Emirates, and Courant Institute of Mathematical Sciences, New York University, New York, New York

Olivier M. Pauluis

Center for Prototype Climate Modeling, New York University Abu Dhabi, Abu Dhabi, United Arab Emirates, and Courant Institute of Mathematical Sciences, New York University, New York, New York

L. Ruby Leung

Atmospheric Sciences and Global Change, Pacific Northwest National Laboratory, Richland, Washington

Fuqing Zhang

Department of Meteorology and Atmospheric Science, and Center for Advanced Data Assimilation and Predictability Techniques, The Pennsylvania State University, University Park, Pennsylvania

(Manuscript received 26 February 2018, in final form 11 June 2018)

ABSTRACT

This study investigates multiscale atmospheric overturning during the 2009 Indian summer monsoon (ISM) using a cloud-permitting numerical model. The isentropic analysis technique adopted here sorts vertical mass fluxes in terms of the equivalent potential temperature of air parcels, which is capable of delineating the atmospheric overturning between ascending air parcels with high entropy and subsiding air parcels with low entropy. The monsoonal overturning is further decomposed into contributions from three characteristic scales: the basinwide ascent over the Indian monsoon domain, the regional-scale overturning associated with synoptic and mesoscale systems, and the convective-scale overturning. Results show that the convective-scale component dominates the upward mass transport in the lower troposphere while the region-scale component plays an important role by deepening the monsoonal overturning. The spatial variability of the convective-scale overturning is analyzed, showing intense convection over the Western Ghats and the Bay of Bengal while the deepest overturning is localized over northern India and the Himalayan foothills. The equivalent potential temperature in convective updrafts is higher over land than over the ocean or coastal regions. There is also substantial variability in the atmospheric overturning associated with the intraseasonal variability. The upward mass and energy transport increase considerably during the active phases of the ISM. A clear northeastward propagation in the peak isentropic vertical mass and energy transport over different characteristic regions can be found during the ISM, which corresponds to the intraseasonal oscillations of the ISM. Altogether, this study further demonstrates the utility of the isentropic analysis technique to characterize the spatiotemporal variations of convective activities in complex atmospheric flows.

---

1. Introduction

The Indian summer monsoon (ISM) is the most striking manifestation of the seasonal cycle associated with a massive shift in the planetary-scale atmospheric overturning on Earth (Trenberth et al. 2000). It is

characterized by extensive rainfall from June to September across the Indian subcontinent and changes in the wind pattern over the Indian Ocean. It is a central aspect of life for over 1 billion people. There is a strong link between the ISM rainfall and the Indian subcontinent's food production, industry, and even its gross domestic product (GDP) (Webster et al. 1998; Goswami et al. 1999; Gadgil and Gadgil 2006; Goswami et al. 2006). The ISM is a complex system that includes atmospheric overturning across various scales. The multiscale overturning and interactions are essential to the ISM dynamics. For example, convergence of moisture driven by large-scale overturning modulates the overturning at the convective scales, while latent heat released within the convective-scale overturning drives the monsoonal large-scale atmospheric circulation (Bhaskaran et al. 1995; Goswami et al. 1999; Kang and Shukla 2006; Chen et al. 2011; Sohn et al. 2012; B. Wang et al. 2015; Goswami and Chakravorty 2017).

The ISM as a whole is generally viewed as a planetary-scale sea-breeze circulation, driven, in part, by the solar forcing and the temperature contrast between ocean and land surfaces (Wu et al. 2012). During the boreal summer, the planetary-scale overturning is dominated by a single cross-equatorial Hadley cell, with a large-scale ascent over the Indian subcontinent and the Bay of Bengal, and a large-scale subsidence over the south Indian Ocean east of Madagascar (Trenberth et al. 2000). Besides the land–sea thermal contrasts, the strength of this planetary-scale overturning is considerably influenced by the blocking and heating effects of the Tibetan Plateau (He et al. 1987; Yanai et al. 1992; Boos and Kuang 2010; Park et al. 2012; Wu et al. 2012), the movements of the subtropical and extratropical westerly jet streams (Krishnamurti and Bhalme 1976), the Indian Ocean dipole (IOD; Sabeerali et al. 2012), and El Niño–Southern Oscillation (ENSO; Goswami and Xavier 2005). As one of the prime manifestations of the seasonal cycle on Earth, the ISM interacts with a broad range of large-scale phenomena.

The atmospheric overturning during the ISM also varies at the synoptic and mesoscales over the Indian subcontinent and the Bay of Bengal, and exhibits variability on the intraseasonal time scale (Taraphdar et al. 2010). The regional-scale atmospheric overturning runs across various spatial scales from hundreds of kilometers (e.g., the organized mesoscale convective systems; Romatschke and Houze 2011; Virts and Houze 2016) to thousands of kilometers (e.g., the monsoon low pressure systems; Krishnamurthy and Ajayamohan 2010; Yanase et al. 2012), with life cycles from hours to days. Inside the regional-scale atmospheric overturning, the convective-scale overturning (through convective clouds) is the main producer of the monsoonal precipitation and greatly influences the onset and maintenance of the ISM (Romatschke et al. 2010).

The moist convective-scale overturning also plays an important role in controlling the moisture, heat, and momentum distribution in the ISM and in the maintenance of the general circulation of the ISM (Das et al. 2002). In correspondence to the strong spatial variations of orography, atmospheric condition, and the underlying surface over the Indian monsoon basin (changing from ocean to coastline to Indian inland region to the Himalayan foothills), the convective-scale overturning (or convective activity) also exhibits strong spatial variability during the ISM (Romatschke and Houze 2011). In addition, the convective activity also shows different behaviors (intensity, depth, width, etc.) during the different intraseasonal phases of the ISM because of the changes of the local atmospheric stability and moisture associated with the monsoon intraseasonal oscillation (MISO; Virts and Houze 2016).

Despite consensus on the multiscale nature of the ISM, the characteristics and the relative contributions to mass and energy transport of the atmospheric overturning at different scales remain a topic of active research. However, to the best of our knowledge, the detailed characteristics of atmospheric overturning across different scales in the ISM have not been examined systematically in the literature. This is at least in part due to limitations of traditional analysis techniques, such as Eulerian averaging, that fail to capture the complicated multiscale atmospheric overturning inside the ISM (Pauluis et al. 2008, 2010). The purpose of this study is to investigate the atmospheric overturning across multiple scales in the ISM using a newly developed isentropic analysis technique (Pauluis and Mrowiec 2013). While the concept of isentropic analysis was introduced by Rossby (1937), the methodology has been recently updated to analyze the convective overturning. Pauluis and Mrowiec (2013) sort the vertical mass transport in terms of the equivalent potential temperature of the air parcels. Using the isentropic analysis, one can readily identify the atmospheric overturning across different scales, all of which are associated with the upward transport of warmer, moister air and the downward transport of colder, drier air, and systematically filtering gravity waves (Pauluis and Mrowiec 2013; Slawinska et al. 2016). This technique has been successfully adopted in previous studies to investigate the thermodynamic cycles in convection (Pauluis 2016), the atmospheric overturning across multiple scales in the Madden–Julian oscillation (MJO; Chen et al. 2018a), the Walker cell (Slawinska et al. 2016), and hurricanes (Mrowiec et al. 2016; Fang et al. 2017; Pauluis and Zhang 2017). Four specific questions will be
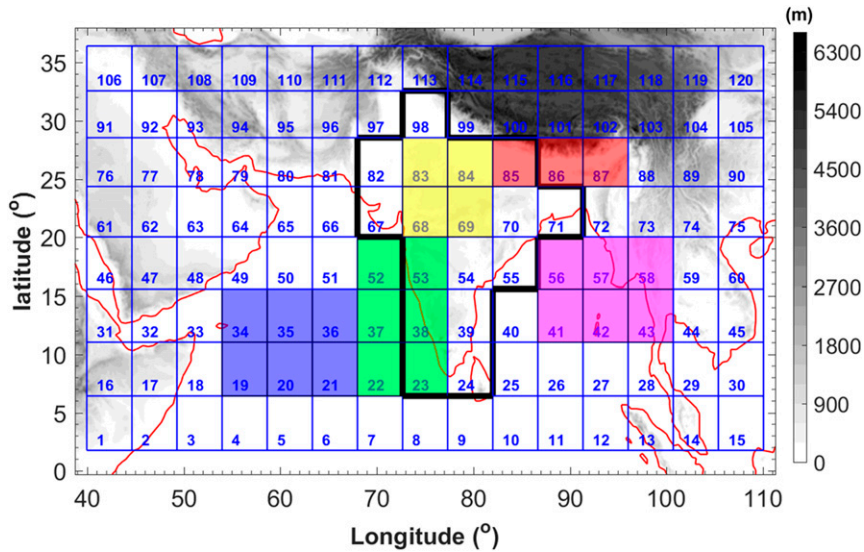
FIG. 1. Model domain used in the WRF simulations with topography (gray scales) and coastlines (red lines). Different subregions are shown by the color shadings: the Arabian Sea (blue); the Western Ghats (green); north India (yellow); the Himalayan foothills (red); the Bay of Bengal (magenta). The black polygon shows the Indian subcontinent.

addressed in this paper through the use of isentropic analysis: What are the statistical characteristics of the ISM atmospheric overturning across different scales? How much do different scales contribute to the total monsoon overturning? As the main producer of the monsoonal precipitation, how does the convective-scale overturning differ across different monsoon subregions? Also, how does the convective-scale overturning vary at the intraseasonal time scales?

Chen et al. (2018b, hereafter C18) simulated the ISM from 2007 to 2011 using a convection-permitting regional model at a gray-zone resolution (9-km grid spacing). The authors compared the model output with multiple observational datasets, and results show that the simulation at the gray-zone resolution can successfully capture many aspects of the ISM atmospheric circulation and precipitation, like the onsets, breaks, and withdraws of the ISMs, in most years. Among the 5-yr simulations, the intraseasonal variations of monsoon rainfall and atmospheric circulation are most realistically reproduced in the year 2009. Using the same model configurations as C18, the current study further performs convection-permitting simulation for the 2009 ISM, which is then used to analyze the atmospheric overturning across multiple scales during the ISM. The experimental setup and analysis methodology are described in section 2. Section 3 analyzes the seasonal-mean atmospheric overturning associated with multiple scales and the spatial variability of the overturning. Because the ISM shows strong intraseasonal variability,

the intraseasonal variations of multiscale atmospheric overturning and the vertical mass and energy transports are analyzed in section 4. Section 5 gives the concluding remarks of the study.

2. Experimental setup and methodology

a. WRF Model setup

The model configuration here is the same as the one used in C18. The Advanced Research WRF Model (Skamarock et al. 2008), version 3.4.1, is used to simulate the atmosphere over the Indian monsoon basin, from $0°$ to $38°$N and from $39°$ to $112°$E (Fig. 1). The horizontal grid spacing is 9 km and no cumulus scheme has been used in the simulation, which is in the so-called gray-zone resolution. Though 9-km grid spacing is not enough to resolve individual convective cells, it is able to capture the statistical characteristics of convective activity, as well as their upscale impact and coupling with large-scale dynamics in regional climate simulations (S. Wang et al. 2015). The convective-scale overturning in the MJO simulated by the regional models at 3- and 9-km horizontal resolutions have been compared in Chen et al. (2018a), and the results show that the depth and strength of convective-scale overturning in both simulations are similar as seen through the isentropic analysis. There are 45 vertical levels for the simulation, with a nominal model top at 20 hPa with nine levels residing typically within the boundary layer. As in C18, an
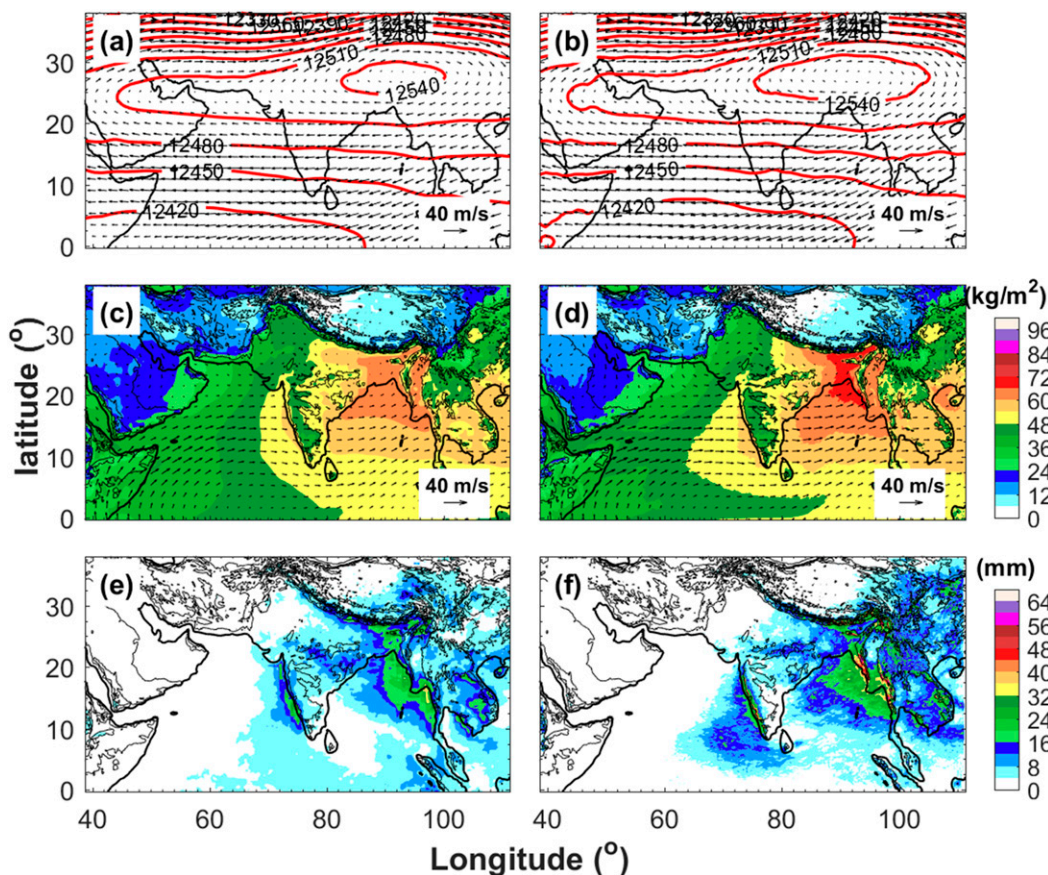
FIG. 2. Monsoon period (JJAS) winds (vectors) and geopotential heights (red contours) at 200-hPa from (a) ERA-Interim and (b) WRF simulation; winds at 850-hPa (vectors) and precipitable water (color shadings) from (c) ERA-Interim and (d) WRF simulation; and daily surface precipitation (color shadings) from (e) TRMM observation and (f) WRF simulation. Topography is shown by the black contours starting at 500 m with a 1000-m interval.

implicit damping scheme (Klemp et al. 2008) has been used in the top 5 km of the model to suppress the vertically propagating gravity waves. The simulation employs the GCM version of the Rapid Radiative Transfer Model (RRTMG) longwave radiation scheme (Iacono et al. 2008), the updated Goddard shortwave scheme (Shi et al. 2010), the unified Noah land surface scheme (Chen and Dudhia 2001), the Asymmetric Convective Model, version 2 (ACM2), boundary layer scheme (Pleim 2007), and the WRF double-moment (WDM) microphysics scheme (Lim and Hong 2010) from WRF, version 3.5.1, with an update on the limit of the shape parameters and terminal speed of snow following S. Wang et al. (2015). The initial and boundary conditions of the simulation are derived from the 6-hourly ERA-Interim (Dee et al. 2011). Sea surface temperature is updated every 6 h using the ERA-Interim SST. The model integration starts from 20 April 2009. For the first 3 days, spectral nudging is applied to relax the horizontal

winds to the ERA-Interim with a zonal wavenumber 0–4 and a meridional wavenumber 0–2 (>2000 km). After 23 April, the model is integrated to 30 October 2009 without any interior nudging. In this study, we focus on the free-running period from 1 June to 30 September (JJAS), which is the Indian summer monsoon season. More details on the model configurations and descriptions can be found in C18.

The model-simulated monsoonal atmospheric circulation and precipitation of the 2009 ISM are verified with ERA-Interim and TRMM observations in Fig. 2. Figures 2a and 2b show the JJAS mean 200-hPa winds and geopotential heights extracted from ERA-Interim and the WRF simulation. The model well captures the Tibetan high-pressure and wind patterns in the upper troposphere, though the Tibetan high-pressure and its associated anticyclonic winds in WRF are slightly stronger than those in ERA-Interim. The strength of the Somali jet in the lower troposphere is a crucial dynamic

factor influencing the strength of the ISM rainfall because it transports moisture from the ocean to the Indian subcontinent and the Bay of Bengal (Joseph and Sijikumar 2004). The WRF Model realistically simulates the geographical position and strength of the Somali jet over the Arabian Sea at 850 hPa (Figs. 2c,d). The spatial distribution and amount of precipitable water in WRF is also similar to that in ERA-Interim, with a slight overestimation over the northern tip of the Bay of Bengal and the southern slope of the Himalayas. The spatial distribution and intensity of JJAS precipitation are well simulated in the WRF Model, while overestimation can be found along the western coastline of Myanmar, the tropical eastern Indian Ocean, and Indochina (Figs. 2e,f). Overall, the WRF Model captures well the seasonal-mean atmospheric circulation and precipitation of the 2009 ISM. A more detailed assessment of the WRF simulations at gray-zone resolution can be found in C18.

b. Isentropic analysis

Because the equivalent potential temperature θ_e of air parcels is conserved during the reversible moist adiabatic process and increases systematically with entropy, the isentropic surfaces can be defined as the surfaces of constant θ_e in the isentropic analysis (Emanuel 1994; Mrowiec et al. 2016; Pauluis 2016; Pauluis and Zhang 2017). We use the frozen equivalent potential temperature following Pauluis [2016, Eq. (2)], defined as the θ_e in

$$(C_{pd} + C_i r_T) \ln \frac{\theta_e}{T_f} = [C_{pd} + r_i C_i + (r_v + r_l) C_l] \ln\left(\frac{T}{T_f}\right) - R_d \ln\left(\frac{P_d}{P_0}\right) + (r_v + r_l)\frac{L_f}{T_f} + r_v\frac{L_v}{T} - r_v R_v \ln H, \quad (1)$$

where T is temperature and T_f is the freezing temperature for water under atmospheric pressure (273.1 K); C_l, C_i, and C_{pd} are the specific heat capacities at constant pressure of liquid water, ice, and dry air, respectively; r_l, r_v, r_i, and r_T represent the mixing ratios for liquid water, water vapor, ice, and total water; R_d and R_v stand for the specific gas constants for dry air and water vapor; L_f is the latent heat of freezing at freezing temperature; L_v is the latent heat of vaporization; and P_0 and P_d are the reference pressure (1000 hPa) and partial pressure of dry air, and H is the relative humidity. The frozen equivalent potential temperature defined following Eq. (1) is typically larger than the θ_e over liquid water (Emanuel 1994) because of the inclusion of the latent heating associated with freezing processes. Isentropic analysis using the equivalent potential temperature with respect to ice can better capture the convective overturning motions above the freezing level (Pauluis 2016).

The isentropic analysis technique developed by Pauluis and Mrowiec (2013) relies on sorting the vertical mass transport in terms of air parcels' θ_e and computes the atmospheric overturning in isentropic coordinates (z, θ_{e0}), which emphasizes the concept that atmospheric overturning at different scales can all be treated as a combination of ascending air parcels with higher entropy and descending air parcels with lower entropy (Pauluis et al. 2010; Mrowiec et al. 2012; Mrowiec et al. 2015; Yamada and Pauluis 2016; Pauluis and Zhang 2017). At the core of the isentropic analysis lies the isentropic distribution of vertical mass transport on a given isentropic slice, which is defined as

$$\langle \rho W \rangle(z, \theta_{e0}) = \frac{1}{PA} \iiint \rho W \delta(\theta_{e0} - \theta_e) a^2 \cos\varphi \, d\varphi \, d\lambda \, dt. \quad (2)$$

Here, ρ is the mass per unit volume and W is the vertical velocity. The isentropic integral $\langle \rho W \rangle$ is expressed in units of ρW per kelvin; θ_{e0} is the mean equivalent potential temperature of a finite θ_e bin; P is the period used for time averaging; A is the area of the averaging domain; a, φ, and λ are Earth's radius (6371 km), latitude, and longitude, respectively; δ is a Dirac function that is equal to $1/\Delta\theta_e$ for θ_e between $\theta_{e0} - 0.5\Delta\theta_e$ and $\theta_{e0} + 0.5\Delta\theta_e$ and 0 elsewhere; and z is the height above the mean sea level (MSL). In practice, the integral in Eq. (2) amounts to summing the vertical mass flux of air parcels at each constant height in finite θ_e bins on an interval of width $\Delta\theta_e$.

The isentropic distribution of vertical mass transport defined by Eq. (2) can be further integrated in the equivalent potential temperature to obtain the isentropic streamfunction

$$\Psi(z, \theta_{e0}) = \int_0^{\theta_{e0}} \langle \rho W \rangle(z, \theta_e') \, d\theta_e'$$

$$= \frac{1}{PA} \iiint \rho W H(\theta_{e0} - \theta_e) a^2 \cos\varphi \, d\varphi \, d\lambda \, dt, \quad (3)$$

in which H is the Heaviside function. From a physical point of view, the definition of isentropic streamfunction would be the net vertical mass flux of all air parcels with an equivalent potential temperature less than θ_{e0} at each given level z. A useful feature of the

isentropic streamfunction is its isolines showing the averaged trajectories of all air parcels with similar equivalent potential temperature in the θ_e–Z phase space (Pauluis 2016). The vertical derivative of the isentropic streamfunction is proportional to the total diabatic heating (Pauluis and Mrowiec 2013). Interested readers can also refer to Pauluis and Mrowiec (2013) and Pauluis (2016) for a more detailed physical interpretation of the isentropic streamfunction.

c. Multiscale decomposition of the vertical mass fluxes

We separate the ISM overturning into the basinwide, regional, and convective scales by using the decomposition methodology introduced in Chen et al. (2018a). First, the WRF domain is divided into 120 subregions with the size of each subregion equal to approximately 450 km × 450 km (50 × 50 model grid points, shown by the blue rectangles in Fig. 1). We used a Mercator grid in the WRF simulation, with a spatial spacing proportional to the cosine of the latitude. Isentropic analyses using different subregion sizes have been compared with each other and the results are shown to be not sensitive to the small changes of the subregion size (not shown here). In each subregion, the vertical mass flux at each model grid point (~9-km resolution) is decomposed into a component at large scales ($\overline{\rho}W_{LS}$) and a convective component (ρW_C) at each model output time (hourly):

$$\rho w = \overline{\rho}W_{LS}(i,j) + \rho W_C. \quad (4)$$

The large-scale component is obtained by averaging the vertical mass flux at all model grid points in the subregion

$$\overline{\rho}W_{LS}(i,j) = \frac{1}{A(i,j)} \iint \rho W a^2 \cos\varphi \, d\varphi \, d\lambda. \quad (5)$$

In above equations, $\overline{\rho}$ is the horizontal-mean mass per unit volume for each subregion; $A(i,j)$ is the area of the corresponding subregion; and a, φ, and λ are Earth's radius (6371 km), latitude, and longitude, respectively. The large-scale vertical mass transport can be further decomposed into a basinwide ascent ($\overline{\rho}W_B$) and regional atmospheric overturning ($\overline{\rho}W_R$) as shown below:

$$\overline{\rho}W_B = \frac{1}{\sum\limits_{j=1}^{NY}\sum\limits_{i=1}^{NX} A(i,j)} \sum_{j=1}^{NY}\sum_{i=1}^{NX} [\overline{\rho}W_{LS}(i,j)A(i,j)], \quad (6)$$

$$\overline{\rho}W_R(i,j) = \overline{\rho}W_{LS}(i,j) - \overline{\rho}W_B. \quad (7)$$

Here, NX and NY are the numbers of subregions in the zonal and meridional directions (15 and 8, shown in

Fig. 1). Using the definitions of isentropic streamfunction, the isentropic streamfunctions associated with basin (Ψ_B), regional (Ψ_R), and convective (Ψ_C) scales are determined by Eq. (3). Thus, the total streamfunction Ψ is decomposed into

$$\Psi(z,\theta_{e0}) = \Psi_B(z,\theta_{e0}) + \Psi_R(z,\theta_{e0}) + \Psi_C(z,\theta_{e0}). \quad (8)$$

With the definitions of Eqs. (6) and (7), Ψ_B is the mean vertical mass flux over the whole Indian monsoon basin and accounts for a basinwide ascending or descending motion during the ISM. The variable Ψ_R represents the atmospheric overturning across different subregions (or across the scales from hundreds of kilometers to thousands of kilometers) in the Indian monsoon basin, which can be treated as the atmospheric overturning at the synoptic and mesoscales, and ρW_C is the atmospheric overturning across different model grid points inside each subregion (or across the scales from kilometers to hundreds of kilometers), which stands for the atmospheric overturning produced by convective activity.

3. Seasonal-mean atmospheric overturning

In this section, the seasonal-mean multiscale atmospheric overturning of the 2009 ISM is investigated in the context of isentropic analysis, with an emphasis on the spatial variability of the convective-scale atmospheric overturning.

a. Atmospheric overturning across multiple scales

Figure 3 shows the isentropic streamfunctions associated with different scales averaged over all 120 subregions of the model domain during the 2009 ISM season (JJAS). The convective-scale isentropic streamfunction is presented in Fig. 3a. The solid black line shows the horizontal-mean profile of equivalent potential temperature. For a statistically steady flow, the streamline of the isentropic streamfunction corresponds to the mean flow in z–θ_e coordinates (Pauluis and Mrowiec 2013; Pauluis 2016). We can see that the convective-scale isentropic streamfunction at each given height is first decreasing with θ_e from the left side of the θ_e axis, which shows air parcels with low entropy descending around the convective core on average. After the streamfunction reaches its minimum at each z level, the convective-scale vertical mass flux changes from negative to positive, and the streamfunction begins to increase with θ_e and finally vanishes at high equivalent potential temperature, which indicates the ascent of warm and moist air parcels at a higher value of θ_e in the center of convection. For the summed convective-scale
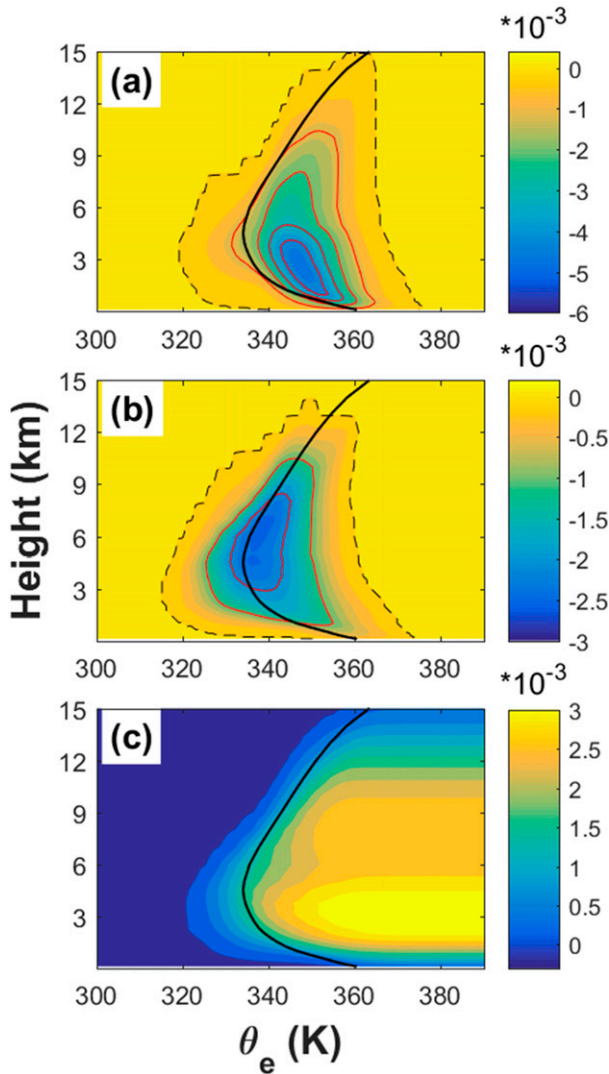
FIG. 3. Isentropic streamfunctions associated with the (a) convective scale, (b) regional scale, and (c) basin scale averaged over all 120 subregions of the model domain during JJAS (color shading; $kg\,m^{-2}\,s^{-1}$). The x axis is the equivalent potential temperature (K) and the y axis is height (km). Isolines of the streamfunctions are shown as red contours starting at $-0.001\,kg\,m^{-2}\,s^{-1}$ with a $-0.001\,kg\,m^{-2}\,s^{-1}$ interval in (a) and (b). The black dashed lines in (a) and (b) show the isolines of $0\,kg\,m^{-2}\,s^{-1}$. The black solid line shows the horizontal-mean profile of equivalent potential temperature averaged over all 120 subregions of the model domain.

overturning, the upward mass transport is always compensated by the downward mass transport based on the definition of Eq. (4), while there is a net upward transport of entropy because the upward-transporting air parcels have higher θ_e than the downward-transporting air parcels on average.

The minimum of the convective-scale streamfunction located at the lower troposphere (near 3 km) reflects that the vertical mass flux is dominated by shallow

convection. The equivalent potential temperature in rising air is about 5–10 K higher than the mean profile of θ_e, which shows that air parcels in the shallow convection are much moister and warmer than the large-scale environment. The outer contours of constant value of the streamfunction (e.g., the dashed contour in Fig. 3a) can be interpreted as the mean thermodynamic trajectories of air parcels in the deep convective-scale overturning. All trajectories are counterclockwise. The air parcels with high θ_e are transported upward from the surface. Before they reach the melting level (at around 5 km), the θ_e decreases slightly with height as a result of the entrainment and mixing of drier air in the updrafts. Above the melting level, θ_e is unchanged before the air parcels reach the top of the deep overturning, which shows that deep convection can transport mass upward without significant dilution above the freezing level. Past the apex point, the air parcels move downward and θ_e decreases by more than 40 K, from 15 km to the melting level, which is induced by radiative cooling. Below the melting level, the equivalent potential temperature of descending air parcels gradually increases as they mix with the detrained cloudy air (refer to Pauluis and Mrowiec 2013).

When compared with the convective-scale overturning that occurs over the equatorial oceans analyzed by Chen et al. (2018a), the convective overturning in the ISM is much deeper, with the top of deep convective-scale overturning around 3 km higher. Also, the deepest updrafts in ISM occur at higher θ_e values (about 15 K higher) than those in the tropical oceans, while their downdrafts have similar values of θ_e. This thermodynamic difference indicates that deep convection in the ISM is more efficient in transporting entropy from the surface to the upper troposphere and has higher convective instability. However, the intensity of shallow convective-scale overturning in the ISM is weaker than that occurring over the tropical oceans (the intensity decreased around 35%), which reflects that the mixing processes in the lower troposphere associated with shallow convection are less vigorous in the ISM.

Figure 3b shows the regional-scale isentropic streamfunction. As defined in Eq. (7), it indicates the collective contributions of organized mesoscale convective systems and synoptic-scale systems to the total atmospheric overturning in the ISM. When compared with the convective-scale overturning, the regional-scale overturning is shallower, with its top 3 km lower. The intensity of the regional-scale overturning is also considerably weaker than the convective-scale overturning (~50% off). The downward mass transport associated with the regional-scale overturning occurs at values of

equivalent temperature lower than at the convective scales and the horizontal-mean profile of θ_e, indicating that the downward mass flux at meso- or synoptic scales occurs through slower subsidence and stronger radiative cooling than the convective scales. The minimum of the regional-scale streamfunction can be found around 6 km, which shows the regional-scale vertical mass transport reaching its maximum in the midtroposphere that corresponds to the height of the maximum updrafts in the organized mesoscale and synoptic systems (Houze 2004; Bosart and Bluestein 2013).

Figure 3c shows the isentropic streamfunction associated with the entire Indian monsoon basin scale. During the ISM, there is a large-scale ascent at higher equivalent potential temperature over the Indian monsoon region, which is compensated by a large-scale subsidence at lower equivalent potential temperature in the winter hemisphere that is outside of the current simulation domain. The boundary conditions from ERA-Interim impose a basinwide mean ascent over the entire simulation domain during JJAS. Hence, the basin-scale streamfunction does not have a closed contour like the convective or regional scales and is positive for the whole troposphere [Based on Eq. (3), the streamfunction is integrated from low equivalent potential temperature. Only the large-scale ascent at high θ_e is captured in the current simulation domain, so the basin-scale streamfunction is positive here]. This basinwide ascent peaking in the lower troposphere shows that the averaged large-scale mean updraft is most prominent under the freezing level. The total vertical mass transport associated with the basinwide ascent over the whole averaging domain (all 120 subregions shown in Fig. 1) is also calculated here. In agreement with the isentropic streamfunction, the basinwide total vertical mass transport peaks in the lower troposphere with a value around $1.8 \times 10^{11}\,\mathrm{kg\,s^{-1}}$, which is comparable to the total mass transport associated with the Hadley cell (Pauluis et al. 2010). In C18, the basin-scale ascent over tropical oceans peaks in the middle troposphere during the MJO active phase. A possible reason why the heights of the large-scale ascent are different over the two regions is that the monsoon domain contains a large inland area, so stronger lowlevel vertical mass transportation could be induced by the stronger orographic lifting and surface heating effects. However, the exact reasons still need future investigation.

b. Spatial variability of atmospheric overturning

One prominent feature of the ISM is its strong spatial variability in convective activity (Romatschke and Houze 2011) due to the various underlying surface and orographic forcing over different regions inside the monsoon domain. In this section, convective-scale atmospheric overturnings in five characteristic regions are compared with each other in the context of the isentropic analysis. These five characteristic regions—the Arabian Sea, the Western Ghats, north India, the Himalayan foothills, and the Bay of Bengal (shown by different color shadings in Fig. 1)—are selected based on their surface and orographic features.

Figures 4b–f show the convective-scale atmospheric overturning averaged over JJAS in the five regions. The convective-scale atmospheric overturning averaged over the whole monsoon domain is presented in Fig. 4a (note the color bar is different in Figs. 4 and 3a). During the ISM, the strongest convective overturning can be found over the coastal regions of the Western Ghats and the Bay of Bengal (Figs. 4c,f). The strong moisture convergence induced by the differential surface frictions and orographic lifting effects along both coastlines could be the reason why stronger convective activity occurs there (Chen et al. 2014, 2017). Such convective overturning also corresponds to intense precipitation (Figs. 2e,f).

The convective streamfunctions over both the Arabian Sea and Western Ghats (Figs. 4b,c) exhibit a pronounced tilt in the lower troposphere. This indicates strong entrainment of dry air in the convective updrafts. These two regions are upstream of the main precipitation regions and are thus directly exposed to the midtropospheric inflow of dry air from the Arabian Peninsula and the Southern Hemisphere (e.g., Krishnamurti et al. 2010). In contrast, the streamline over the continental region and the Bay of Bengal exhibits a weaker tilt in the lower troposphere, which indicates a lesser impact of entrainment on the convective-scale overturning in these regions.

The isentropic streamfunctions over the inland regions (Figs. 4c,e) are shifted toward higher values of equivalent potential temperature, indicating that updrafts have higher energy content over land than over the oceans. This shift is likely due to a lower heat capacity of the land surface, so that the absorbed solar radiation directly contributes to increasing the energy content of the air in the boundary layer. This leads to a stronger diurnal cycle and higher θ_e values over land than over the ocean (Dai 2001). The convective-scale atmospheric overturning over the inland regions is also deeper than that in the coastal regions, reaching an altitude of up to 15 km over the Himalayan foothills. The entrainment in the convective updraft in the lower troposphere is much weaker over the inland regions (Figs. 4c,e), which reflects that the convective vertical motions are stronger in these regions.
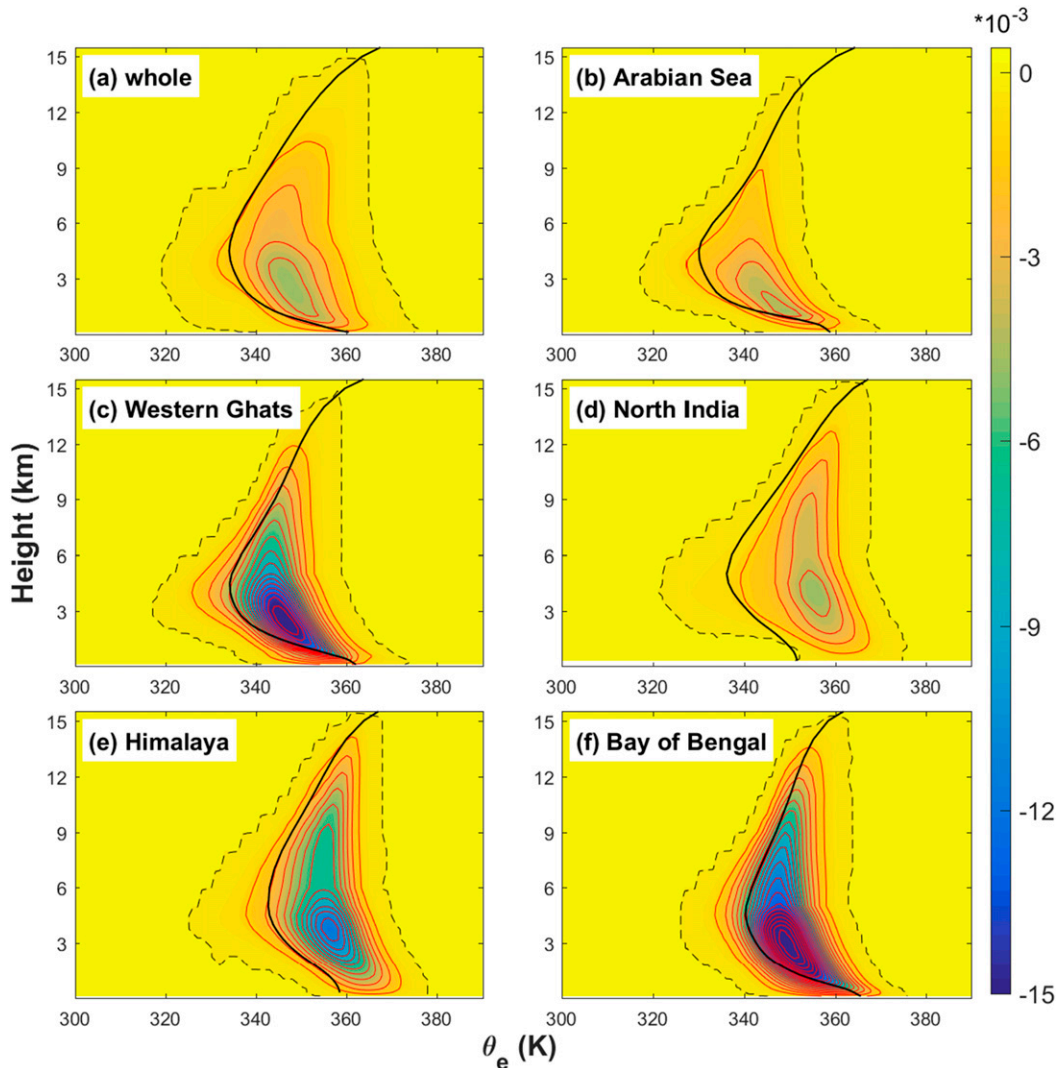
FIG. 4. Isentropic streamfunctions associated with convective scale (color shading; $kg\,m^{-2}\,s^{-1}$) averaged over (a) all 120 subregions of the model domain; (b) the Arabian Sea; (c) the Western Ghats; (d) north India; (e) the Himalayan foothills; (f) the Bay of Bengal during JJAS. The x axis is equivalent potential temperature (K) and the y axis is height (km). Isolines of the streamfunctions are shown as red contours starting at $-0.001\,kg\,m^{-2}\,s^{-1}$ with a $-0.001\,kg\,m^{-2}\,s^{-1}$ interval. The black dashed lines show the isolines of $0\,kg\,m^{-2}\,s^{-1}$. The black solid line shows the horizontal-mean profile of equivalent potential temperature averaged over (a) all 120 subregions of the model domain and (b)–(f) different subregions.

Because of the stronger orographic blocking and lifting effects, the intensity of convective overturning over the Himalayan foothills (Fig. 4d) is around 2 times stronger than that in north India. These results are consistent with the long-term satellite observations (Romatschke et al. 2010; Romatschke and Houze 2011), which show that convection occurring over the inland regions is deeper than that occurring over the ocean area during the ISM, and with the analysis of Nie et al. (2010), who show the presence of very high values of θ_e ($\sim$360 K) over northern India during the ISM. Hence our results

demonstrate that the isentropic analysis technique provides a direct way for us to link the vertical mass and energy transports to the monsoon precipitation. Through the isentropic analysis, the thermodynamic cycles of atmospheric overturning can be extracted and compared between different monsoon subregions. This comparison clearly shows the influences of surface types and orography on the convective-scale overturning in the ISM.

To further elucidate the spatial variations of the vertical mass transport associated with convective-scale overturning, the isentropic upward mass transport
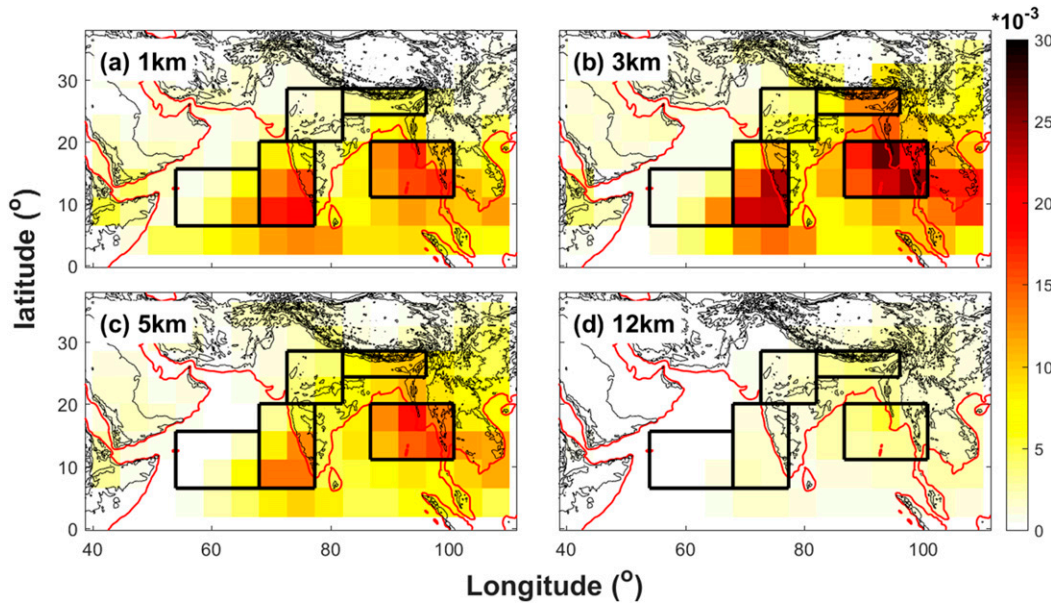
FIG. 5. Isentropic upward mass transport $(\mathrm{kg\,m^{-2}\,s^{-1}})$ associated with the convective scale during JJAS (color shading) at (a) 1-, (b) 3-, (c) 5-, and (d) 12-km altitude. Different subregions are shown by black boxes and coastlines are shown by red lines.

is defined below following Slawinska et al.'s (2016) Eq. (10):

$$M(z) = \max_{\theta_e}[\Psi(z, \theta_{e0})] - \min_{\theta_e}[\Psi(z, \theta_{e0})]. \qquad (9)$$

The max and min are the maximum and minimum of streamfunction in the θ_e coordinate at a given height. Figure 5 shows the spatial distributions of the convective upward mass transport at different levels during the ISM. Consistent with the convective-scale isentropic streamfunction (Fig. 3a), the upward mass transport at the convective scale is dominated by shallow convection that peaks around 3 km (Fig. 5b). Strong upward mass flux can still be found around the freezing level (Fig. 5c), while the vertical mass transport produced by the convective activity is relatively weak in the upper troposphere over the whole monsoon domain (Fig. 5d, one magnitude weaker than the mass transport in the lower troposphere). The spatial distribution of the convective-scale upward mass transport follows the same pattern as the accumulated monsoon precipitation (Figs. 2e,f), indicating that the convective-scale activity is the main producer of the monsoon rainfall, which is consistent with the long-term satellite observations (Romatschke and Houze 2011). As in the analysis of the subregional isentropic streamfunctions in Fig. 4, the convective-scale isentropic upward mass flux is strongest over the Western Ghats and the Bay of Bengal and weakest over the Arabian Sea below the melting level. Above the melting

level, the convective upward mass transport decreases more dramatically over the Western Ghats and the Bay of Bengal and is almost at the same values as that in north India and the Himalayan foothills. It indicates that the convective-scale atmospheric overturning over the coastal subregions is more dominated by shallow convective activity than that over the inland subregions, which is consistent with the discussions of Fig. 4 and satellite observations (Romatschke and Houze 2011).

One advantage of the isentropic analysis is that it offers an efficient way to characterize the thermodynamic properties of atmospheric overturning with a two-stream approximation (Pauluis and Mrowiec 2013). The spatial distributions of the isentropic-mean equivalent potential temperature in the mean convective-scale updraft are further investigated to assess the vertical energy transport associated with the convective-scale atmospheric overturning in the ISM. First, the mean updraft of convective-scale atmospheric overturning in each subregion at each model output time (output every hour) is defined as

$$M^+(z, t) = \int_{-\infty}^{\infty} \langle \rho W_C \rangle H(\langle \rho W_C \rangle) \, d\theta_e. \qquad (10)$$

Here, t is the model integration time, z is altitude, and H is a Heaviside step function. The isentropic-mean equivalent potential temperature in the mean convective updraft θ_e^+ is further defined as
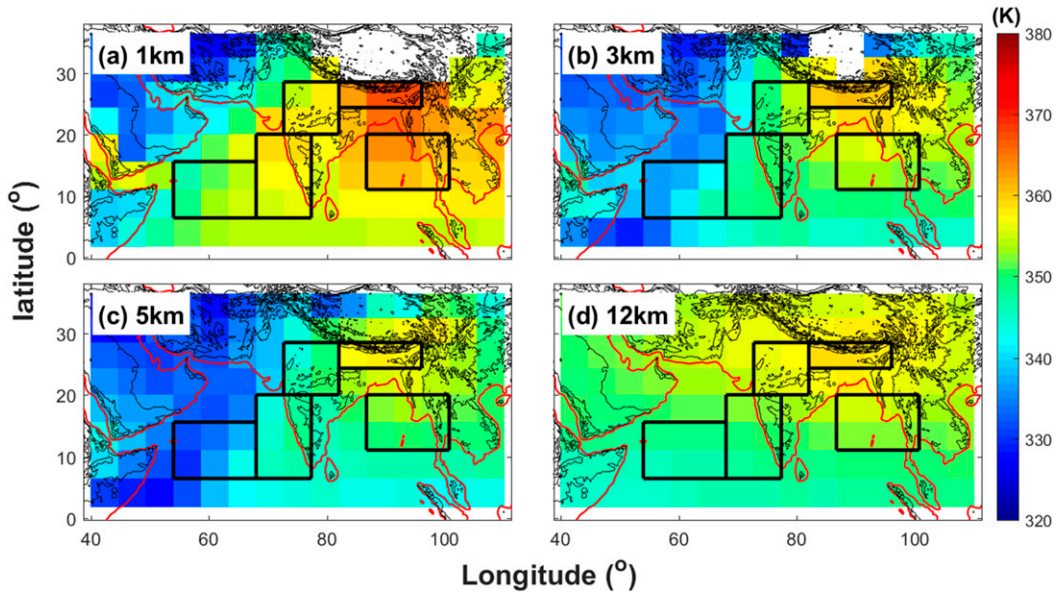
FIG. 6. Isentropic-mean equivalent potential temperature (K) in the mean convective-scale updraft (color shading) at (a) 1-, (b) 3-, (c) 5-, and (d) 12-km altitude during JJAS. Different subregions are shown by black boxes and coastlines are shown by red lines.

$$\theta_e^+(z,t) = \frac{1}{M^+} \int_{-\infty}^{\infty} \langle \rho W_C \theta_e \rangle H(\langle \rho W_C \rangle) \, d\theta_e'. \quad (11)$$

The spatial distributions of the seasonal averaged θ_e^+ at different altitudes are shown in Fig. 6. We can find that, over all subregions in the monsoon domain, θ_e in the convective updraft decreases with height in the lower troposphere because of the entrainment and mixing of drier air (Figs. 6a–c) and increases slightly with height above the melting level because of the increase in the proportion of deep convective updraft (Fig. 6d). The θ_e decrease in the lower troposphere (e.g., from 1 to 5 km) is more significant over the Western Ghats, Bay of Bengal, and Arabian Sea (close to 30 K) than over inland regions (around 13 K), which indicates a weaker convective updraft and a stronger entrainment over the oceanic and coastal regions as the isentropic stream-functions shown in Fig. 4. Among all five characteristic regions, θ_e^+ is highest over the foothills of the Himalayas, which shows that the entropy of upward convective mass transport is highest on the south slope of the Himalayas where anomalous deep convective activity frequently occurs during the ISM (Romatschke et al. 2010).

4. Intraseasonal variations of atmospheric overturning

The ISM exhibits strong low-frequency variability in the form of "active" and "break" spells of monsoon rainfall (Goswami and Ajayamohan 2001) with a dominant mode on a time scale of 30–60 days (Sikka and Gadgil 1980; Yasunari 1981). This low-frequency mode is also known as the MISO, which affects the seasonal-mean strength of the ISM and is characterized by a northeastward propagation of enhanced or suppressed precipitation from the Indian Ocean to the Himalayan foothills (Jiang et al. 2004). The intraseasonal oscillation of monsoonal precipitation is closely related to the changes in the atmospheric circulations (Sabeerali et al. 2017). C18 shows that the WRF Model at the gray-zone resolution can well simulate the intraseasonal variations of the ISM rainfall and atmospheric circulations. In this section, the intraseasonal variability of multiscale atmospheric overturning in the ISM is studied in the context of the isentropic analysis, with an emphasis on the spatial and temporal variations of the convective-scale atmospheric overturning, which has a close relationship with the monsoon rainfall.

a. Vertical mass transport across multiple scales

Figure 7a shows the temporal evolution of daily precipitation averaged over the Indian subcontinent (shown by the black polygon in Fig. 1) from TRMM observation (black line) and the WRF simulation (blue line). Generally speaking, the WRF simulation well simulates the mean strength and intraseasonal variation of the monsoon rainfall. The rainfall over the Indian subcontinent begins to increase gradually from the beginning of June and reaches an active phase in July. Then the monsoon rainfall decreases quickly and a clear
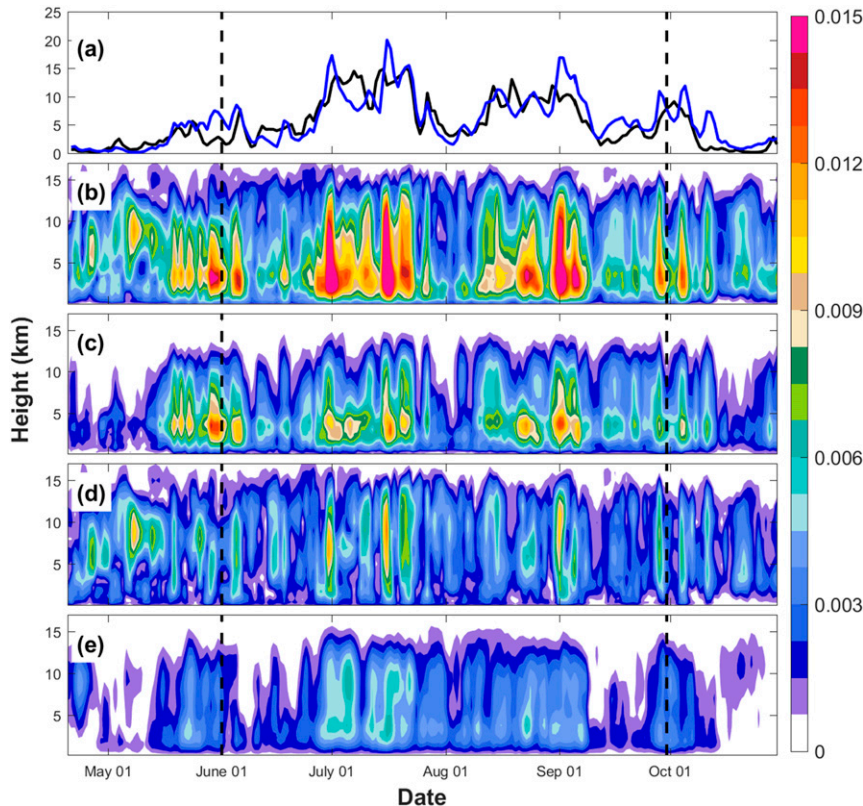
FIG. 7. (a) Evolution of daily precipitation averaged over the Indian subcontinent from TRMM (black line) and WRF (blue line). A 5-day moving average is applied to the time series. Evolution of isentropic upward mass transports (color shading; $kg\,m^{-2}\,s^{-1}$) associated with (b) all scales, (c) convective scale, (d) regional scale, and (e) basin scale averaged over the Indian subcontinent. The black dashed lines show the JJAS period.

break phase can be found at the beginning of August. In the next 3 weeks, the rainfall over the Indian subcontinent increases again and reaches another active phase around the beginning of September. Another break phase of the monsoon rainfall occurs in mid-September, and one weak active phase can be found at the end of September. Withdrawal of the ISM occurs at the beginning of October.

The evolution of the isentropic upward mass transport associated with all spatial scales averaged over the Indian subcontinent is shown in Fig. 7b. The atmospheric overturning evolves systematically with the monsoon rainfall (Fig. 7a): it intensifies gradually from the beginning of June and weakens gradually at the beginning of October, which corresponds to the onset and the end of the ISM, respectively. The active and break phases of the monsoon rainfall correspond to the intensification and weakening of the atmospheric overturning, implying that the intraseasonal variation of the monsoon rainfall is closely associated with the changes in atmospheric circulations. The increase in atmospheric overturning during the active phase of the ISM

is primarily associated with an increase in the contributions by the convective-scale and regional-scale overturning (Figs. 7c,d). In contrast, the contribution from basinwide updraft is relatively small while some modest enhancements can still be found during the active phases of the ISM (Fig. 7e).

The convective-scale upward mass transport peaks in the lower troposphere (Fig. 7c). Around 64% of the total mass transport below the melting level is contributed by the convective-scale overturning during JJAS, which indicates the preponderance of shallow convective activity in the ISM. Most deep convective overturning occurs during the ISM active phase, which is related to the more unstable atmospheric environment during the time (Romatschke et al. 2010). Both the shallow and deep atmospheric overturning associated with the convective scale are enhanced significantly during the active phase of the ISM. Compared to the ISM break phase, the convective-scale upward mass transport is enhanced by around 250% in the lower troposphere and by as high as 260% above the melting level during the ISM active phase. In agreement with the enhancement of the
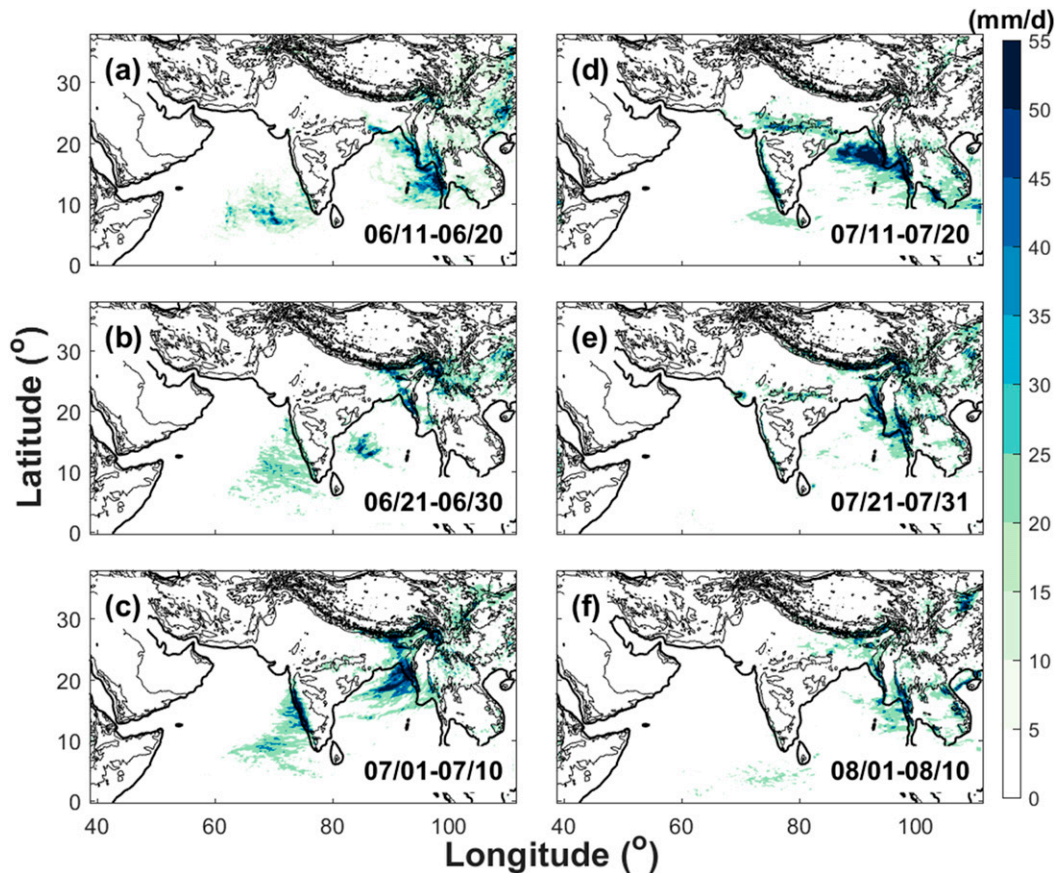
FIG. 8. Spatial distribution of daily average rainfall in (a) 11–20 Jun; (b) 21–30 Jun; (c) 1–10 Jul; (d) 11–20 Jul; (e) 21–31 Jul; and (f) 1–10 Aug in the WRF simulation. Topography is shown by the black contours starting at 500 m with a 1000-m interval.

convective-scale atmospheric overturning (or convective activities), precipitation over the Indian subcontinent also increases by 142% during the ISM active phase.

The vertical mass transport produced by the regional-scale overturning has comparable magnitude, but is relatively weaker than the one associated with the convective scale (Fig. 7d). It peaks in the middle troposphere, as shown by the isentropic streamfunction (Fig. 3b). During the ISM season, close to 43% of the total vertical mass transport in the middle and upper troposphere is contributed by the regional-scale atmospheric overturning, which indicates that synoptic and mesoscale systems play an important role in deepening the monsoonal overturning. The upward mass transport associated with the region scale is enhanced by 159% during the active phase of the ISM, reflecting more synoptic or mesoscale systems occurring during the ISM active phase, for example, the monsoon low pressure systems (Krishnamurthy and Ajayamohan 2010).

The vertical mass transport associated with the basin-scale circulation (Fig. 7e) is much smaller than that associated with the convective and regional scales. During JJAS, less than 25% of the total vertical mass transport in the troposphere is contributed by the basinwide ascent. However, the contribution of the basin-scale overturning in the ISM is still higher when compared to that of the MJOs (less than 20%, Chen et al. 2018a). The intraseasonal oscillation of the basin-scale overturning is not as significant as that associated with the convective and regional scales. However, intensifications of the basin-scale ascent can still be found during the active phases of the ISM, especially around 1 July (Fig. 7e). It shows that the heating of the atmosphere by convective activity can intensify the regional Hadley circulation during the ISM active phase (Goswami and Chakravorty 2017).

b. Atmospheric overturning at the convective scales

The spatial and temporal variations of the convective-scale atmospheric overturning associated with the MISO are studied in more detail in this section. Figure 8 shows
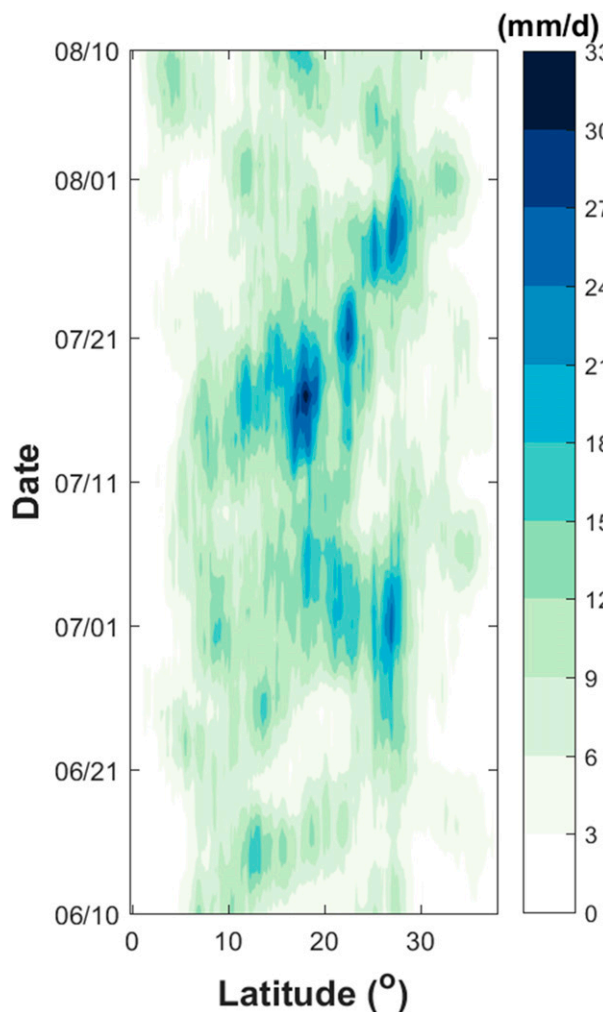
FIG. 9. Time–latitude diagram of daily surface rainfall averaged over the longitude 60°–110°E.

the daily average rainfall for each 10-day period starting from 11 June to 10 August 2019, which includes the onset of the ISM and a complete cycle of the MISO. During the onset stage of the ISM, enhanced rainfall moves from the Arabian Sea to the Indian subcontinent in June, and strong precipitation can be found along the western coastline of the subcontinent (Figs. 8a,b). From early to mid-July, precipitation over the Indian inland region increases gradually and the ISM reaches an active phase during 11–20 July (Figs. 8c,d). During the active phase, the enhanced rainfall forms a northwest–southeast line that stretches from the west coast of the Indian subcontinent to south of Indochina, which is similar to the active phase composited feature obtained from long-term satellite and surface observations (Sabeerali et al. 2017). The monsoon rainfall over north India begins to decrease at the end of July (Fig. 8e) and the ISM

reaches a break phase in early August (Fig. 8f). However, precipitation over the Himalayan foothills reaches an active phase in these 20 days (Figs. 8e,f), which corresponds to the northeastward-propagating feature of the MISO. The onset of the ISM and northward propagation of MISO are further shown in Fig. 9. Similar to Fig. 8, the Hovmöller diagram clearly shows that the onset of the ISM is around June 20, with surface precipitation gradually increasing over the Western Ghats. The ISM reaches an active phase during 11–21 July. A clear northward propagation of MISO can be found from 11 July to 4 August, with strong surface rainfall propagating from the west coast of the Indian subcontinent to the Himalayan foothills. At the same time, a break phase of ISM can be found in early August, when surface rainfall over the Indian subcontinent is suppressed (Figs. 8 and 9).

Figures 10 shows the 10-day evolutions of the isentropic upward mass transport associated with the convective-scale atmospheric overturning. Before the onset of the ISM, strong convective mass transport is still located over the Arabian Sea area (Fig. 10a). Active convective mass transport (Fig. 10a) and precipitation (Fig. 8a) can also be found over the Bay of Bengal at this time. With the onset of the ISM, the convective mass transport intensifies dramatically over the Western Ghats, indicating strong convective activity occurring along the coastline and producing heavy rainfall over the region. However, the convective activity in north India is still very weak (Fig. 10b). In the next 20 days, the convective upward mass transport over north India increases gradually with convective activity over the Western Ghats weakening (Figs. 10c,d). During the active phase of the ISM, the convective upward mass transport over north India and the Bay of Bengal both reach their strongest stage of the 2-month period (Fig. 10d), which is consistent with the enhanced rainfall line stretching from the west coast of the Indian subcontinent to south of Indochina at that time (Fig. 8d). From the end of July to the beginning of August, the convective activity over north India and the Bay of Bengal weakens while the convective mass transport over the Himalayan foothills increases considerably (Figs. 10e,f), in agreement with the variations of surface rainfall (Figs. 8e,f).

Figure 11 shows the intraseasonal variation of the isentropic-mean equivalent potential temperature in the mean convective-scale updraft at 3-km altitude. The equivalent potential temperature of convective updraft is higher over the inland regions in general and peaks over the Himalayan foothills. Over the Arabian Sea, θ_e^+ is highest before the onset of the ISM (Fig. 11a). The θ_e^+ over the Western Ghats reaches its highest
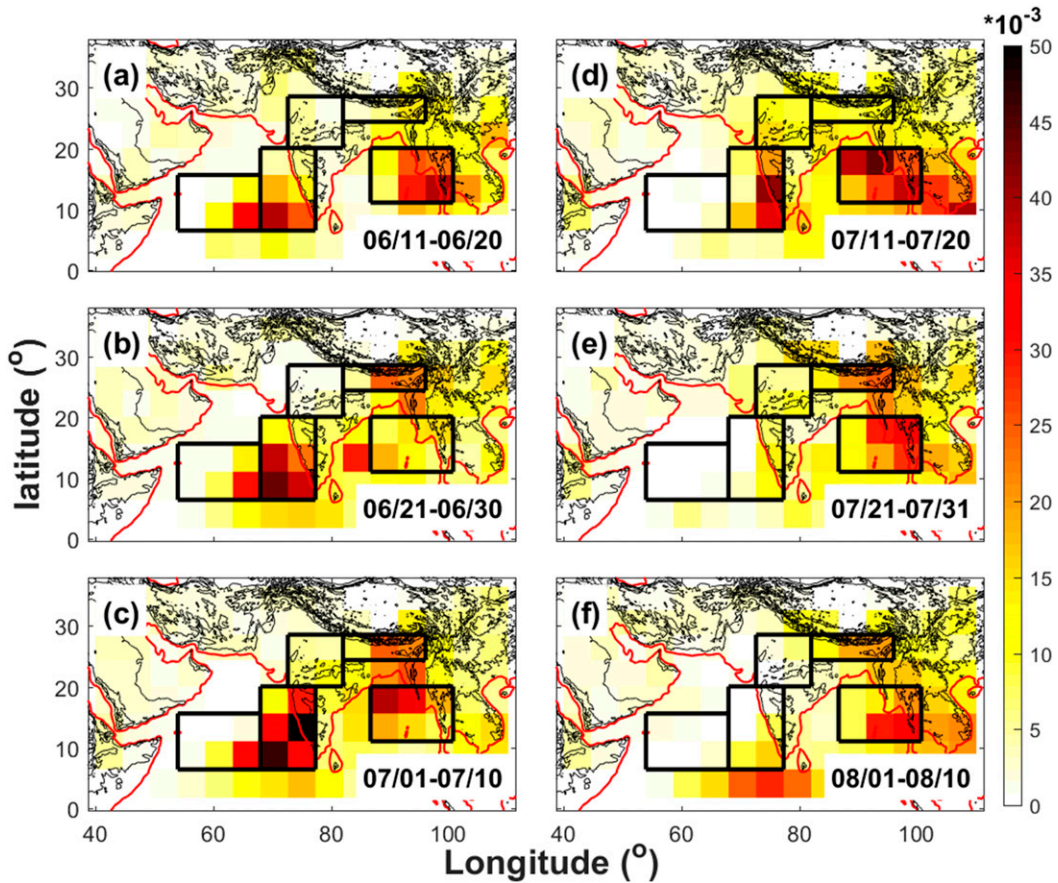
FIG. 10. Averaged isentropic upward mass transport (kg m^{-2} s^{-1}) associated with the convective scale at 3 km in (a) 11–20 Jun; (b) 21–30 Jun; (c) 1–10 Jul; (d) 11–20 Jul; (e) 21–31 Jul; and (f) 1–10 Aug. Different subregions are shown by black boxes and coastlines are shown by red lines.

value near the onset of the ISM (Figs. 11b,c) but it is reduced considerably during the later stage of the ISM. The reduction in θ_e^+ over the Western Ghats indicates that advection of dry air is probably the primary factor leading to the diminishing of convection there (Krishnamurti et al. 2010). Over north India and the Bay of Bengal, the highest values of θ_e^+ can be found during the active phase of the ISM (Fig. 11d), which is consistent with the more intense convection and precipitation over these two regions during this period (Figs. 8d and 10d). It is noteworthy that the highest value of θ_e^+ over the Himalayan foothills occurs during the break phase of the ISM (Fig. 11f). It is in agreement with the enhancement of rainfall over the region during the break phase (Fig. 8f), which is associated with deeper convective-scale overturning and stronger latent heating (will be shown in Fig. 12). The isentropic analysis shows not only that the evolution of the convective mass and entropy transports capture the northeastward propagation of the MISO, but also indicates regional differences in the behavior of convection.

The 10-day evolution of isentropic streamfunction associated with the convective-scale circulations averaged over five characteristic regions is presented in Fig. 12. Only the isentropic streamfunctions smaller than −0.001 kg m^{-2} s^{-1} are shown here. The black solid lines in Fig. 12 show the horizontal-mean profile of θ_e. Similar to the seasonal-mean streamfunction shown in Fig. 4, on average, the convective-scale atmospheric overturning over the oceanic regions is shallower and with lower entropy compared with that over the inland regions. Obvious intraseasonal variations of the convective-scale overturning can be found over all five characteristic regions. Over the Arabian Sea (the first row in Fig. 12), the convective-scale atmospheric overturning is strongest before the onset of the ISM (11–20 June), with its depth exceeding 10-km altitude. The convective-scale overturning over the Arabian Sea weakens dramatically after the onset of the ISM and convective activity is mostly concentered below 3 km during the ISM. The convective-scale overturning over the Western Ghats (the second row in Fig. 12) reaches its strongest phase
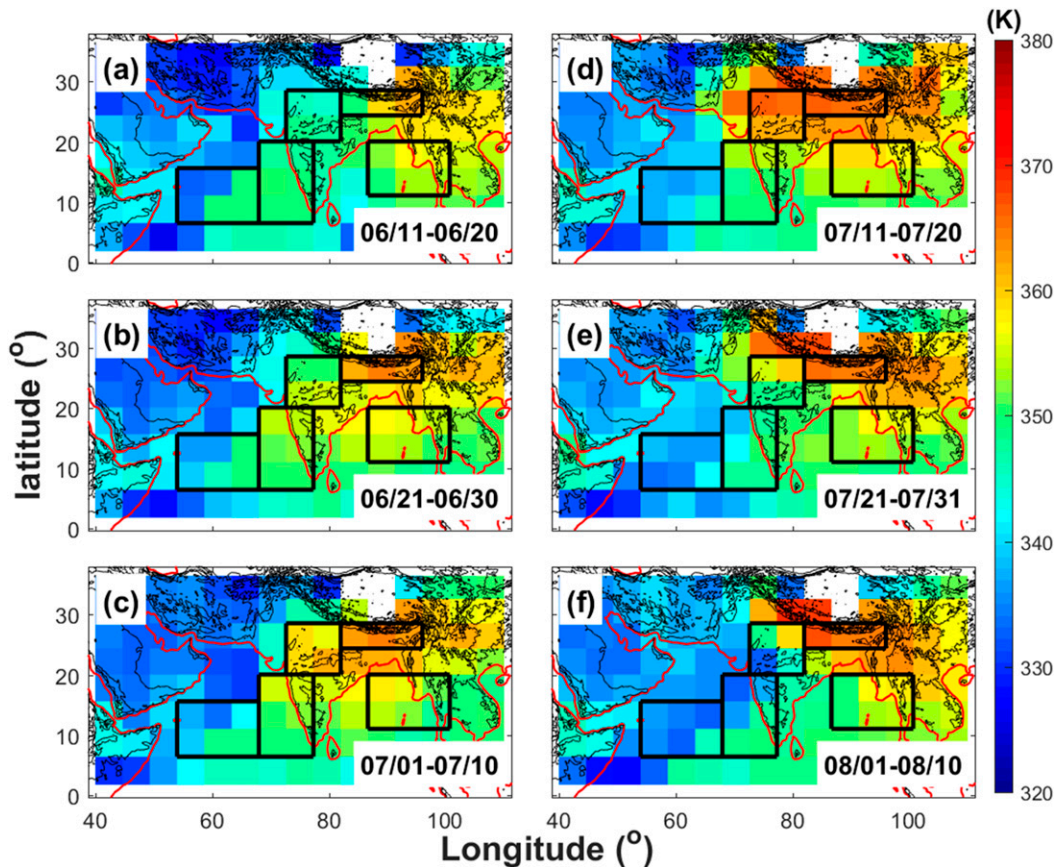
FIG. 11. Isentropic-mean equivalent potential temperature (K) in the mean convective-scale updraft at 3 km (color shading) in (a) 11–20 Jun; (b) 21–30 Jun; (c) 1–10 Jul; (d) 11–20 Jul; (e) 21–31 Jul; and (f) 1–10 Aug. Different subregions are shown by black boxes and coastlines are shown by red lines.

near the onset of the ISM (21 June–10 July). The depth and intensity of the convective-scale overturning decreases considerably during the break phase of the ISM (21 July–10 August), with most convective-scale overturning occurring under the melting level, which shows that the precipitation over the Western Ghats during the ISM break phase is dominated by the warm rain processes. The convective-scale overturning in north India (the third row in Fig. 12) is very weak (one order of magnitude weaker than the seasonal-mean strength) before the onset of the ISM and intensifies dramatically during the ISM active phase (11–20 July). In the active phase, deep convective-scale overturning can transport air from the near-surface to the upper troposphere (~14 km) with little loss of the entropy of the air parcels (or weak entrainment effects), indicating that extreme deep convection occurs frequently over north India during the ISM active phase. The convective-scale overturning over north India weakens notably during the ISM break phase (1–10 August). Because of the strong orographic lifting effect, extreme

deep convection with the top exceeding 14-km altitude occurs frequently over the Himalayan foothills during the ISM (the fourth row in Fig. 12). This result is consistent with the long-term TRMM observations (Romatschke et al. 2010; Romatschke and Houze 2011). The convective-scale overturning over the Himalayan foothills reaches its strongest stage during the break phase of the ISM (1–10 August). The intraseasonal variation of the convective-scale atmospheric overturning over the Bay of Bengal (the fifth row in Fig. 12) is similar to that in north India, with its strongest stage occurring during the active phase of the ISM (11–20 July). However, the intensity of the convective-scale overturning in the Bay of Bengal is much stronger than that in north India on average, which corresponds to stronger precipitation over the region. The strongest stages of the convective-scale overturning over different regions clearly show the northeastward propagation of the ISM (from the Arabian Sea to the Western Ghats to north India and the Bay of Bengal to the Himalayan foothills), which again shows that the isentropic analysis
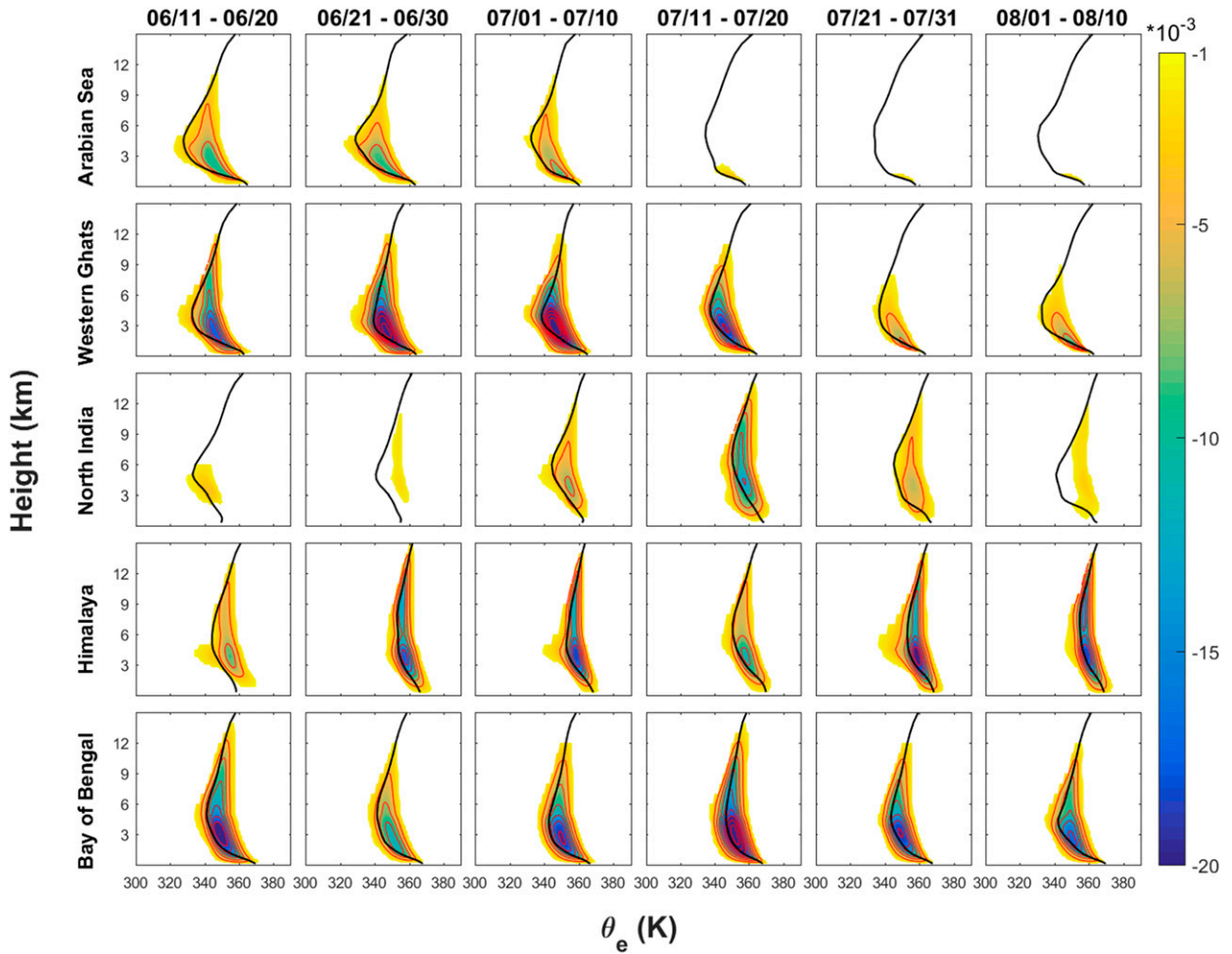
FIG. 12. Isentropic streamfunctions associated with convective scale averaged over different subregions (rows) and different periods (columns). Only the streamfunctions smaller than $-0.001\ \mathrm{kg\ m^{-2}\ s^{-1}}$ are shown. Isolines of the streamfunctions are shown as red contours starting at $-0.002\ \mathrm{kg\ m^{-2}\ s^{-1}}$ with a $-0.001\ \mathrm{kg\ m^{-2}\ s^{-1}}$ interval. The black solid lines show the mean profile of equivalent potential temperature averaged over different subregions during different periods.

is a useful tool for investigating the propagation and variation of the atmospheric overturning associated with the MISO.

5. Summary and discussion

In this study, we analyzed the multiscale atmospheric overturning during the 2009 ISM. The ISM is simulated with the WRF Model using the same configuration as described in C18. Isentropic analysis is adopted in this study to investigate the spatial and temporal variations of the atmospheric overturning across multiple scales in the ISM, with a special emphasis on the convective-scale overturning, which is closely related to the monsoon precipitation.

The atmospheric overturning of the 2009 ISM is decomposed into three contributors: a basinwide ascent

(basin scale), a region-scale overturning that is associated with synoptic and organized mesoscale systems (region scale), and a convective contribution (convective scale). Our analysis shows that atmospheric overturning over the Indian subcontinent is dominated by the convective and regional scales. The vertical mass transport in the lower troposphere is mainly contributed by the convective-scale circulations, while the mass transport associated with the regional scales reaches its maximum in the midtroposphere, and thus enables the atmosphere to transport energy to higher altitude. Both the convective- and region-scale overturnings of the ISM exhibit a strong intraseasonal variation, with their strengths peaking during the active phase of the ISM. The basin-scale overturning is much weaker (contributes less than 25% of the total vertical mass transport) than that due to the synoptic/mesoscale systems or convection.

Because of the different underlying surface characters and orographic forcings, the convective-scale atmospheric overturning in the ISM shows a strong spatial variation. Five characteristic regions are selected (the Arabian Sea, the Western Ghats, north India, the Himalayan foothills, and the Bay of Bengal) and the seasonal-mean convective-scale atmospheric overturning occurring in these regions is compared in the context of the isentropic analysis in this study. On average, the convective-scale overturning over the inland regions (north India and the Himalayan foothills) is deeper ($\sim$2–3 km) than that over the oceanic and coastal regions (the Arabian Sea, the Western Ghats, and the Bay of Bengal). The convective-scale overturning over the inland regions also shows higher entropy than that over the oceans and coastlines. It results in a stronger convective upward energy transport in north India and the Himalayan foothills. However, shallow convective-scale overturning is most active along the coastlines (the Western Ghats and the Bay of Bengal), indicating that strong warm rain processes occur over the coastal regions. These results derived from the isentropic analysis are consistent with the long-term TRMM observations (Romatschke and Houze 2011).

Besides spatial variations, the convective-scale atmospheric overturning also shows a strong intraseasonal variation, which is closely related to the intraseasonal oscillations of the monsoon rainfall. Isentropic analysis shows that both the vertical mass and energy transports over the Indian subcontinent are stronger during the ISM active phase than in the ISM break phases. The strongest phases of the convective-scale atmospheric overturning averaged over different characteristic regions show that the isentropic analysis can well capture the northeastward propagation of the MISO and its associated variations of the atmospheric overturning. The convective-scale overturning in north India and the Bay of Bengal peaks during the ISM active phase, while the convective-scale overturning over the Himalayan foothills reaches its strongest stage in the ISM break phase.

Our analysis shows that fluctuations of convective activity during the ISM differ markedly from the variations of convection during an MJO event studied with the same methodology by Chen et al. (2018a). Indeed, the MJO appears primarily as a displacement of the center of convective activity, without any substantial change in the thermodynamic properties of the updrafts. In contrast, in the ISM, we find that the regional shift in convective activity is also associated with very large changes in the equivalent potential temperature of the rising air parcels. It is consistent with the long-term satellite observations, which show that the behaviors of convective activity have a strong spatial variability in the ISM (Romatschke et al. 2010). In particular, our

simulation indicates that convection over the Himalayan foothills regularly exhibits equivalent potential temperature above 360 K, an exceptionally high value that is more typical of tropical storms. Air parcels ascending at such high entropy can substantially contribute to the excess production of kinetic energy by the atmospheric circulation (Pauluis 2016). The isentropic analysis can provide new insights on how changes in the atmospheric circulation are related to the changes in convective activity, a question central to our understanding of the summer monsoon. Future studies will extend this to different seasons and years, including the interannual variability. Recent studies show that warm SST anomalies leading the MISO convection may play a very important role in the northeastward propagation of the MISO (e.g., Fu et al. 2003). Our high-resolution simulation provides an opportunity for future studies to further investigate the impacts of SST anomalies on the MISO propagation.

REFERENCES

Bhaskaran, B., J. F. B. Mitchell, J. R. Lavery, and M. Lal, 1995: Climatic response of the Indian subcontinent to doubled CO_2 concentrations. *Int. J. Climatol.*, **15**, 873–892, https://doi.org/10.1002/joc.3370150804.

Boos, W. R., and Z. Kuang, 2010: Dominant control of the South Asian monsoon by orographic insulation versus plateau heating. *Nature*, **463**, 218–222, https://doi.org/10.1038/nature08707.

Bosart, L. F., and H. B. Bluestein, Eds., 2013: *Synoptic–Dynamic Meteorology and Weather Analysis and Forecasting: A Tribute to Fred Sanders. Meteor. Monogr.*, No. 55, Amer. Meteor. Soc., 440 pp.

Chen, F., and J. Dudhia, 2001: Coupling an advanced land surface–hydrology model with the Penn State–NCAR MM5 modeling system. Part I: Model implementation and sensitivity. *Mon. Wea. Rev.*, **129**, 569–585, https://doi.org/10.1175/1520-0493(2001)129<0569:CAALSH>2.0.CO;2.

Chen, G.-S., Z. Liu, S. C. Clemens, W. L. Prell, and X. Liu, 2011: Modeling the time-dependent response of the Asian summer monsoon to obliquity forcing in a coupled GCM: A PHASEMAP sensitivity experiment. *Climate Dyn.*, **36**, 695–710, https://doi.org/10.1007/s00382-010-0740-3.

Chen, X., K. Zhao, and M. Xue, 2014: Spatial and temporal characteristics of warm season convection over Pearl River delta region, China, based on 3 years of operational radar data. *J. Geophys. Res. Atmos.*, **119**, 12 447–12 465, https://doi.org/10.1002/2014JD021965.

——, F. Zhang, and K. Zhao, 2017: Influence of monsoonal wind speed and moisture content on intensity and diurnal variations of the mei-yu season coastal rainfall over south China. *J. Atmos. Sci.*, **74**, 2835–2856, https://doi.org/10.1175/JAS-D-17-0081.1.

——, O. M. Pauluis, and F. Zhang, 2018a: Atmospheric overturning across multiple scales of an MJO event during the CINDY/DYNAMO campaign. *J. Atmos. Sci.*, **75**, 381–399, https://doi.org/10.1175/JAS-D-17-0060.1.

——, ——, and ——, 2018b: Regional simulation of Indian summer monsoon intraseasonal oscillations at gray-zone resolution. *Atmos. Chem. Phys.*, **18**, 1003–1022, https://doi.org/10.5194/acp-18-1003-2018.

Dai, A., 2001: Global precipitation and thunderstorm frequencies. Part II: Diurnal variations. *J. Climate*, **14**, 1112–1128, https://doi.org/10.1175/1520-0442(2001)014<1112:GPATFP>2.0.CO;2.

Das, S., A. K. Mitra, G. R. Iyengar, and J. Singh, 2002: Skill of medium-range forecasts over the Indian monsoon region using different parameterizations of deep convection. *Wea. Forecasting*, **17**, 1194–1210, https://doi.org/10.1175/1520-0434(2002)017<1194:SOMRFO>2.0.CO;2.

Dee, D. P., and Coauthors, 2011: The Era-Interim reanalysis: Configuration and performance of the data assimilation system. *Quart. J. Roy. Meteor. Soc.*, **137**, 553–597, https://doi.org/10.1002/qj.828.

Emanuel, K. A., 1994: *Atmospheric Convection.* Oxford University Press, 580 pp.

Fang, J., O. Pauluis, and F. Zhang, 2017: Isentropic analysis on the intensification of Hurricane Edouard (2014). *J. Atmos. Sci.*, **74**, 4177–4197, https://doi.org/10.1175/JAS-D-17-0092.1.

Fu, X., B. Wang, T. Li, and J. P. McCreary, 2003: Coupling between northward-propagating, intraseasonal oscillations and sea surface temperature in the Indian Ocean. *J. Atmos. Sci.*, **60**, 1733–1753, https://doi.org/10.1175/1520-0469(2003)060<1733:CBNIOA>2.0.CO;2.

Gadgil, S., and S. Gadgil, 2006: The Indian monsoon, GDP and agriculture. *Econ. Polit. Wkly.*, **41**, 4887–4895.

Goswami, B. N., and R. S. Ajayamohan, 2001: Intraseasonal oscillations and interannual variability of the Indian summer monsoon. *J. Climate*, **14**, 1180–1198, https://doi.org/10.1175/1520-0442(2001)014<1180:IOAIVO>2.0.CO;2.

——, and P. K. Xavier, 2005: ENSO control on the South Asian monsoon through the length of the rainy season. *Geophys. Res. Lett.*, **32**, L18717, https://doi.org/10.1029/2005GL023216.

——, and S. Chakravorty, 2017: Dynamics of the Indian summer monsoon climate. *Oxford Research Encyclopedia*, https://doi.org/10.1093/acrefore/9780190228620.013.613.

——, V. Krishnamurthy, and H. Annmalai, 1999: A broad-scale circulation index for the interannual variability of the Indian summer monsoon. *Quart. J. Roy. Meteor. Soc.*, **125**, 611–633, https://doi.org/10.1002/qj.49712555412.

——, G. Wu, and T. Yasunari, 2006: The annual cycle, intraseasonal oscillations, and roadblock to seasonal predictability of the Asian summer monsoon. *J. Climate*, **19**, 5078–5099, https://doi.org/10.1175/JCLI3901.1.

He, H., J. W. McGinnis, Z. Song, and M. Yanai, 1987: Onset of the Asian summer monsoon in 1979 and the effect of the Tibetan Plateau. *Mon. Wea. Rev.*, **115**, 1966–1995, https://doi.org/10.1175/1520-0493(1987)115<1966:OOTASM>2.0.CO;2.

Houze, R. A., Jr., 2004: Mesoscale convective systems. *Rev. Geophys.*, **42**, RG4003, https://doi.org/10.1029/2004RG000150.

Iacono, M. J., J. S. Delamere, E. J. Mlawer, M. W. Shephard, S. A. Clough, and W. D. Collins, 2008: Radiative forcing by long-lived greenhouse gases: Calculations with the AER radiative transfer models. *J. Geophys. Res.*, **113**, D13103, https://doi.org/10.1029/2008JD009944.

Jiang, X., T. Li, and B. Wang, 2004: Structures and mechanisms of the northward propagating boreal summer intraseasonal oscillation. *J. Climate*, **17**, 1022–1039, https://doi.org/10.1175/1520-0442(2004)017<1022:SAMOTN>2.0.CO;2.

Joseph, P. V., and S. Sijikumar, 2004: Intraseasonal variability of the low-level jet stream of the Asian summer monsoon. *J. Climate*, **17**, 1449–1458, https://doi.org/10.1175/1520-0442(2004)017<1449:IVOTLJ>2.0.CO;2.

Kang, I.-S., and J. Shukla, 2006: Dynamic seasonal prediction and predictability of the monsoon. *The Asian Monsoon*, B. Wang, Ed., Springer Berlin Heidelberg, 585–612.

Klemp, J. B., J. Dudhia, and A. D. Hassiotis, 2008: An upper gravity-wave absorbing layer for NWP applications. *Mon. Wea. Rev.*, **136**, 3987–4004, https://doi.org/10.1175/2008MWR2596.1.

Krishnamurti, T. N., and H. N. Bhalme, 1976: Oscillations of a monsoon system. Part I. Observational aspects. *J. Atmos. Sci.*, **33**, 1937–1954, https://doi.org/10.1175/1520-0469(1976)033<1937:OOAMSP>2.0.CO;2.

——, A. Thomas, A. Simon, and V. Kumar, 2010: Desert air incursions, an overlooked aspect, for the dry spells of the Indian summer monsoon. *J. Atmos. Sci.*, **67**, 3423–3441, https://doi.org/10.1175/2010JAS3440.1.

Krishnamurthy, V., and R. S. Ajayamohan, 2010: Composite structure of monsoon low pressure systems and its relation to Indian rainfall. *J. Climate*, **23**, 4285–4305, https://doi.org/10.1175/2010JCLI2953.1.

Lim, K.-S. S., and S.-Y. Hong, 2010: Development of an effective double-moment cloud microphysics scheme with prognostic cloud condensation nuclei (CCN) for weather and climate models. *Mon. Wea. Rev.*, **138**, 1587–1612, https://doi.org/10.1175/2009MWR2968.1.

Mrowiec, A. A., C. Rio, A. M. Fridlind, A. S. Ackerman, A. D. Del Genio, O. M. Pauluis, A. C. Varble, and J. Fan, 2012: Analysis of cloud-resolving simulations of a tropical mesoscale convective system observed during TWP-ICE: Vertical fluxes and draft properties in convective and stratiform regions. *J. Geophys. Res.*, **117**, D19201, https://doi.org/10.1029/2012JD017759.

——, O. M. Pauluis, A. M. Fridlind, and A. S. Ackerman, 2015: Properties of a mesoscale convective system in the context of an isentropic analysis. *J. Atmos. Sci.*, **72**, 1945–1962, https://doi.org/10.1175/JAS-D-14-0139.1.

——, ——, and F. Zhang, 2016: Isentropic analysis of a simulated hurricane. *J. Atmos. Sci.*, **73**, 1857–1870, https://doi.org/10.1175/JAS-D-15-0063.1.

Nie, J., W. R. Boos, and Z. Kuang, 2010: Observational evaluation of a convective quasi-equilibrium view of monsoons. *J. Climate*, **23**, 4416–4428, https://doi.org/10.1175/2010JCLI3505.1.

Park, H.-S., J. C. H. Chiang, and S. Bordoni, 2012: The mechanical impact of the Tibetan Plateau on the seasonal evolution of the South Asian monsoon. *J. Climate*, **25**, 2394–2407, https://doi.org/10.1175/JCLI-D-11-00281.1.

Pauluis, O. M., 2016: The mean air flow as Lagrangian dynamics approximation and its application to moist convection. *J. Atmos. Sci.*, **73**, 4407–4425, https://doi.org/10.1175/JAS-D-15-0284.1.

——, and A. A. Mrowiec, 2013: Isentropic analysis of convective motions. *J. Atmos. Sci.*, **70**, 3673–3688, https://doi.org/10.1175/JAS-D-12-0205.1.

——, and F. Zhang, 2017: Reconstruction of thermodynamic cycles in a high-resolution simulation of a hurricane. *J. Atmos. Sci.*, **74**, 3367–3381, https://doi.org/10.1175/JAS-D-16-0353.1.

——, A. Czaja, and R. Korty, 2008: The global atmospheric circulation on moist isentropes. *Science*, **321**, 1075–1078, https://doi.org/10.1126/science.1159649.

——, ——, and ——, 2010: The global atmospheric circulation in moist isentropic coordinates. *J. Climate*, **23**, 3077–3093, https://doi.org/10.1175/2009JCLI2789.1.

Pleim, J. E., 2007: A combined local and nonlocal closure model for the atmospheric boundary layer. Part I: Model description and testing. *J. Appl. Meteor. Climatol.*, **46**, 1383–1395, https://doi.org/10.1175/JAM2539.1.

Romatschke, U., and R. A. Houze, 2011: Characteristics of precipitating convective systems in the South Asian monsoon. *J. Hydrometeor.*, **12**, 3–26, https://doi.org/10.1175/2010JHM1289.1.

——, S. Medina, and R. A. Houze Jr., 2010: Regional, seasonal, and diurnal variations of extreme convection in the South Asian region. *J. Climate*, **23**, 419–439, https://doi.org/10.1175/2009JCLI3140.1.

Rossby, C.-G., 1937: Isentropic analysis. *Bull. Amer. Meteor. Soc.*, **18**, 201–209.

Sabeerali, C. T., S. A. Rao, R. S. Ajayamohan, and R. Murtugudde, 2012: On the relationship between Indian summer monsoon withdrawal and Indo-Pacific SST anomalies before and after 1976/1977 climate shift. *Climate Dyn.*, **39**, 841–859, https://doi.org/10.1007/s00382-011-1269-9.

——, R. S. Ajayamohan, D. Giannakis, and A. J. Majda, 2017: Extraction and prediction of indices for monsoon intraseasonal oscillations: An approach based on nonlinear Laplacian spectral analysis. *Climate Dyn.*, **49**, 3031–3050, https://doi.org/10.1007/s00382-016-3491-y.

Shi, J. J., and Coauthors, 2010: WRF simulations of the 20–22 January 2007 snow events over eastern Canada: Comparison with in situ and satellite observations. *J. Appl. Meteor. Climatol.*, **49**, 2246–2266, https://doi.org/10.1175/2010JAMC2282.1.

Sikka, D. R., and S. Gadgil, 1980: On the maximum cloud zone and the ITCZ over Indian, longitudes during the southwest monsoon. *Mon. Wea. Rev.*, **108**, 1840–1853, https://doi.org/10.1175/1520-0493(1980)108<1840:OTMCZA>2.0.CO;2.

Skamarock, W. C., and Coauthors, 2008: A description of the Advanced Research WRF version 3. NCAR Tech. Note NCAR/TN-475+STR, 113 pp., https://doi.org/10.5065/D68S4MVH.

Slawinska, J., O. Pauluis, A. J. Majda, and W. W. Grabowski, 2016: Multiscale interactions in an idealized Walker cell: Analysis with isentropic streamfunctions. *J. Atmos. Sci.*, **73**, 1187–1203, https://doi.org/10.1175/JAS-D-15-0070.1.

Sohn, S.-J., Y.-M. Min, J.-Y. Lee, C.-Y. Tam, I.-S. Kang, B. Wang, J.-B. Ahn, and T. Yamagata, 2012: Assessment of the long-lead probabilistic prediction for the Asian summer monsoon precipitation (1983–2011) based on the APCC multimodel system and a statistical model. *J. Geophys. Res.*, **117**, D04102, https://doi.org/10.1029/2011JD016308.

Taraphdar, S., P. Mukhopadhyay, and B. N. Goswami, 2010: Predictability of Indian summer monsoon weather during active and break phases using a high resolution regional model. *Geophys. Res. Lett.*, **37**, L21812, https://doi.org/10.1029/2010GL044969.

Trenberth, K. E., D. P. Stepaniak, and J. M. Caron, 2000: The global monsoon as seen through the divergent atmospheric circulation. *J. Climate*, **13**, 3969–3993, https://doi.org/10.1175/1520-0442(2000)013<3969:TGMAST>2.0.CO;2.

Virts, K. S., and R. A. Houze, 2016: Seasonal and intraseasonal variability of mesoscale convective systems over the South Asian monsoon region. *J. Atmos. Sci.*, **73**, 4753–4774, https://doi.org/10.1175/JAS-D-16-0022.1.

Wang, B., J.-Y. Lee, and B. Xiang, 2015: Asian summer monsoon rainfall predictability: A predictable mode analysis. *Climate Dyn.*, **44**, 61–74, https://doi.org/10.1007/s00382-014-2218-1.

Wang, S., A. H. Sobel, F. Zhang, Y. Q. Sun, Y. Yue, and L. Zhou, 2015: Regional simulation of the October and November MJO events observed during the CINDY/DYNAMO field campaign at gray zone resolution. *J. Climate*, **28**, 2097–2119, https://doi.org/10.1175/JCLI-D-14-00294.1.

Webster, P. J., V. O. Magaña, T. N. Palmer, J. Shukla, R. A. Tomas, M. Yanai, and T. Yasunari, 1998: Monsoons: Processes, predictability, and the prospects for prediction. *J. Geophys. Res.*, **103**, 14 451–14 510, https://doi.org/10.1029/97JC02719.

Wu, G., Y. Liu, B. He, Q. Bao, A. Duan, and F.-F. Jin, 2012: Thermal controls on the Asian summer monsoon, **2**, 404, https://doi.org/10.1038/srep00404.

Yamada, R., and O. Pauluis, 2016: Momentum balance and Eliassen–Palm flux on moist isentropic surfaces. *J. Atmos. Sci.*, **73**, 1293–1314, https://doi.org/10.1175/JAS-D-15-0229.1.

Yanai, M., C. Li, and Z. Song, 1992: Seasonal heating of the Tibetan Plateau and its effects on the evolution of the Asian summer monsoon. *J. Meteor. Soc. Japan*, **70**, 319–351, https://doi.org/10.2151/jmsj1965.70.1B_319.

Yanase, W., M. Satoh, H. Taniguchi, and H. Fujinami, 2012: Seasonal and intraseasonal modulation of tropical cyclogenesis environment over the Bay of Bengal during the extended summer monsoon. *J. Climate*, **25**, 2914–2930, https://doi.org/10.1175/JCLI-D-11-00208.1.

Yasunari, T., 1981: Structure of an Indian summer monsoon system with around 40-day period. *J. Meteor. Soc. Japan*, **59**, 336–354.